JOURNAL OF SPACECRAFT AND ROCKETS
Vol. 43, No. 1, January–February 2006

Computational Aerodynamic Analysis of Capsule Configurations Toward the Development of Reusable Rockets

Keiichiro Fujimoto*
University of Tokyo, Tokyo 133-8656, Japan
and
Kozo Fujii†
Japan Aerospace Exploration Agency, Kanagawa 229-8510, Japan

Flowfields around Apollo-type conical configurations are numerically simulated by Reynolds-averaged Navier–Stokes computations at a wide range of angles of attack under subsonic through supersonic flows. Effects of the configuration parameters on the aerodynamic characteristics and their flow mechanisms were clarified based on the computed results. It turns out that the aerodynamic characteristics are mainly influenced by the separation position of the flow, the pressure level behind the body, and the wind-side high pressures. The shoulder radius has a great influence on the pressure level behind the body and the separation position, so that the aerodynamic characteristics, especially at base-first conditions, significantly change. The drag coefficient at base-first conditions becomes small for configuration with the large shoulder radius because of the increase of the lee-side pressure level. At both nose-first and base-first conditions, the fineness ratio has great influence on the location and the pressure level of the wind-side high pressures, which appear on the windward cone part, so that the lift, drag, and pitching-moment coefficients significantly change.

Nomenclature

C_A = axial-force coefficient, axial force/$(q_\infty S_{\text{ref}})$
C_D = drag coefficient, drag/$(q_\infty S_{\text{ref}})$
C_L = lift coefficient, lift/$(q_\infty S_{\text{ref}})$
C_{ma} = pitching-moment coefficient computed about theoretical apex
C_N = normal-force coefficient, normal force/$(q_\infty S_{\text{ref}})$
$D_{\max}$ = maximum diameter of the body
L/D = lift-to-drag ratio C_L/C_D
M = Mach number
Pr = Prandtl number
q = dynamic pressure
Re = Reynolds number based on $D_{\max}$
S_{ref} = reference area
x, y, z = Cartesian body axes
α = angle of attack, deg
γ = specific heat ratio
μ = viscosity

Subscripts

inf(∞) = freestream condition
lam = laminar value
max = maximum value
tur = turbulent value
$\alpha 0$ = aerodynamic coefficients at $\alpha = 0$ deg
$\alpha 180$ = aerodynamic coefficients at $\alpha = 180$ deg

I. Introduction

A WIDE variety of space-access concepts has been proposed and studied over the past two decades, aiming to reduce launch costs and improve reliability and flexibility of space transportation systems. In 1994, NASA headquarters concluded that one option recommended for the access to space was the development of a fully reusable, all rocket-propelled, single-stage-to-orbit (SSTO) launch vehicle.[1] The X-33 demonstrator was based on the concept of the SSTO, which is a vertical takeoff and horizontal landing vehicle with lifting body.[2] The Delta Clipper has extensively demonstrated the reusability of the SSTO rocket and the flight capability of a vertical takeoff and vertical landing (VTVL) vehicles.[3] At the Institute of Space and Astronautical Science/Japan Aerospace Exploration Agency (ISAS/JAXA) in Japan, ground and flight tests of VTVL-SSTO rocket system are presently conducted for the establishment of the basic technologies.[4] There are two types of entry flight concepts: nose-first and base-first entry, and each has its own advantage. The configuration of such a VTVL-SSTO rocket will be totally different from conventional rocket configurations, and its flight trajectory includes a wide range of flow conditions: subsonic through hypersonic at a variety of angles of attack. In addition, high L/D and high maneuverability are the key issues for the design of the vehicle's configuration. Various aerodynamic considerations should be made to realize the atmospheric flight. Under the development of the Delta Clipper, comprehensive experimental aerodynamic research is performed at McDonnell Douglas and at the NASA Langley Research Center.[5] Mach and Reynolds numbers, nose bluntness, and the aerodynamic fin effects on the aerodynamic forces and longitudinal stability are extensively investigated in these experiments. At the ISAS/JAXA, computational fluid dynamics (CFD)-based aerodynamic analysis is carried out supporting development of the VTVL-SSTO rocket system. In the preliminary design stage of the vehicle configuration, CFD analysis has strong advantages as it supplies a wide range of aerodynamic data, whereas only limited data can be obtained by the wind-tunnel experiments. CFD has another advantage that it can supply the flowfield information behind the aerodynamic characteristics. CFD analysis is already an established essential tool in the design process of aircraft based on the fact that a certain level of reliability has been established by the accumulation of the flow simulations. In the other fields, however, CFD reliability has not been established, and this is also true for the space launch vehicles.

Presented as Paper 2003-0912 at the AIAA 41st Aerospace Sciences Meeting, Reno, NV, 6–9 January 2003; received 13 September 2004; revision received 18 January 2005; accepted for publication 18 January 2005.

*Graduate Student, Department of Aeronautics and Astronautics. Student Member AIAA.

†Professor, Institute of Space and Astronautical Science. Fellow AIAA.

Therefore, an initial part of this research is to investigate the capability of CFD aerodynamic prediction for basic SSTO rocket configurations.[6–8] This study starts with flow computations over the Apollo configuration at a wide range of angles of attack under the subsonic to supersonic flows. Apollo configuration was chosen because there are large amount of fine experimental data available, and the objective of this study is to provide basic aerodynamic information about simple configuration for conceptual design. Computed aerodynamic coefficients agree well with the experimental data, and it was concluded that CFD aerodynamic prediction is reliable for the preliminary design stage.

Effects of configuration parameters on the aerodynamic characteristics are numerically investigated as a second part of this research. This paper presents the results of the aerodynamic analysis at a wide variety of attack angles under the subsonic through supersonic flows. The flow mechanism behind the aerodynamic characteristics is also presented.

II. Numerical Method

A. Geometries

Body configurations considered in the present study are shown in Fig. 1. Apollo configuration is set to be the same as described in Ref. 9. Case 1 has two times larger radius of the cone apex than that of Apollo. Case 2b has five times larger shoulder radius, and case 3b has the cone half-angle of 21 deg, and other parameters are the same as Apollo.

To investigate the effects of the configuration parameters on $(C_D)_{\alpha 0}$ and $(C_D)_{\alpha 180}$, two additional sets of configurations are considered. One series of configurations has a larger shoulder radius than that of Apollo: $Rs = 0.10$, 0.15, 0.20, and 0.25 for case Rs01, Rs02, Rs03, and Rs04. Another series of configurations has a smaller cone half-angle than that of Apollo: 15.0, 21.0, and 27.0 for case TH15, TH21, and TH27. Case TH21, corresponds to case 3b. All geometries are nondimensionalized by $D_{\max}$.

B. Body System of Axes

As shown in Fig. 2, $\alpha = 180$ deg corresponds to base-first, and $\alpha = 0$ deg corresponds to nose-first condition. An anticlockwise rotation corresponds to the direction of decreasing α. The pitching-moment coefficient C_{ma} is computed about the theoretical apex. The aerodynamic forces and moments are defined as shown in Fig. 2.

C. Computational Domain and Grid

Flowfields are assumed to be symmetric about the pitch plane ($y = 0$). Therefore, the computational domain covers half of the body. The computational grid consists of 53 equispaced circumferential planes ($\Delta\phi = 3.6$ deg) extending around half of the body, whose topology is O-O type. In each circumferential plane, the grid contains 61 radial points between the body and the computational outer boundary and 91 axial points between the nose and the rear end of the body. Minimum grid spacing near the wall is 3.0×10^{-5}, and the computational domain ranges from -10.0 to $+10.0$ in all directions as shown in Fig. 3.

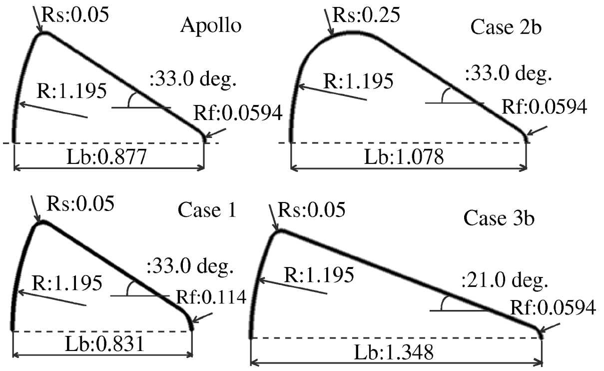

Fig. 1 Configuration parameters of the body.

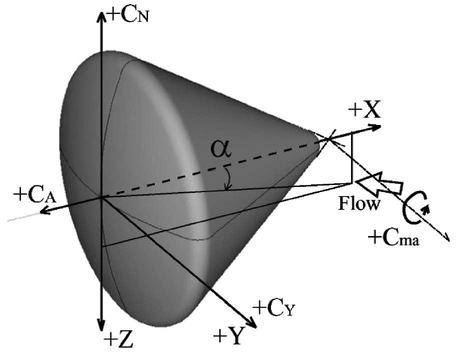

Fig. 2 Sketch showing body system of axes.

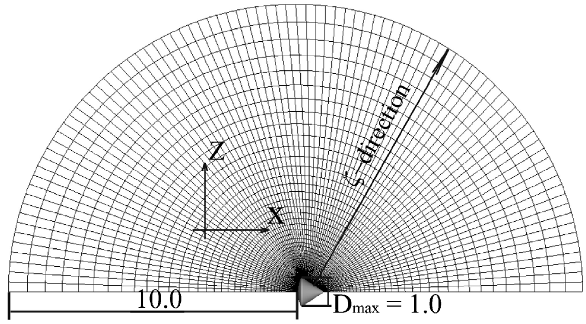

Fig. 3 Entire view of the computational grid.

D. Flow Solver

The basic equations are the three-dimensional compressible full Navier–Stokes equations:

$$\frac{\partial \hat{Q}}{\partial t} + \frac{\partial \hat{E}}{\partial \xi} + \frac{\partial \hat{F}}{\partial \eta} + \frac{\partial \hat{G}}{\partial \zeta} = 0 \tag{1}$$

Length, density, velocity components and viscosity ρ, u, v, w, μ are normalized by $D_{\max}$, ρ_∞, freestream speed of sound c_∞, and freestream molecular viscosity μ_∞, respectively. The pressure, density, and velocity components are related to the total energy for an ideal gas by the following equation:

$$p = (\gamma - 1)^{\frac{1}{2}} e - \tfrac{1}{2}\rho^{i} u^2 + v^2 + w^{2^{\phi^{\frac{3}{4}}}} \tag{2}$$

The metrics are evaluated using second-order central-difference formulas for the interior points. Numerical fluxes for the convective terms are evaluated by the simple high-resolution upwind scheme,[10] extended to high-order space accuracy by third-order upwind-biased MUSCL interpolation[11] based on the primitive variables. Viscous terms are evaluated by second-order central differencing. The lower–upper alternating direction implicit (LU-ADI) factorized implicit algorithm[12] is used for the time integration with a globally constant time step with no inner iterations. The flowfield is considered to be fully turbulent, and the Baldwin–Lomax turbulence model[13] is applied.

The computational code is based on the authors' in-house code, which has been applied for many compressible flowfields including vortical flow,[14] unsteady flow,[15] and transonic flow.[16] Discussions on the detail and accuracy of the computational code are given in the references.

E. Flow Parameters

Flow conditions are listed in Table 1. Because one of the major issues of aerodynamic design is the aerodynamic characteristics under subsonic through supersonic flows, the aerodynamic characteristics of this speed regime are mainly focused. The γ, Pr_{lam}, Pr_{tur}, and μ_{lam} are fixed to be 1.4, 0.72, 0.90, and 1.0 in all of the computations.

Table 1 Flow conditions for calculations for Apollo

Parameter	Value
M_∞	0.7, 0.9, 1.2, 2.0
Re_∞	1.0×10^6
α, deg	0, 15, 24, 36, 45, 60, 70, 80, 90 100, 110, 120, 130, 144, 156, 165, 180

F. Data Processing

Aerodynamic forces on the body are strongly influenced by flow unsteadiness behind the body. Especially at subsonic and transonic conditions, the lee-side pressure significantly varies in time because of the unsteady recirculating wake flow. Therefore, all of the aerodynamic coefficients in the following discussion are based on the time-averaged physical variables.

III. Results and Discussion

CFD aerodynamic analysis of four types of configurations, Apollo, cases 1, 2b, and 3b, is conducted for both the nose-first ($\alpha = 0$–90 deg) and base-first conditions ($\alpha = 90$–180 deg). Although the flow computations were carried out at $M_\infty = 0.7$, 0.9, 1.2, and 2.0, the discussion of the results under two flow conditions, $M_\infty = 0.9$ and 1.2, is presented because of the space limitation. All of the computed aerodynamic coefficients are available in Ref. 17. Computed aerodynamic coefficients for Apollo, cases 2b and 3b, are shown in Figs. 4a–4c for $M_\infty = 0.9$ and in Figs. 5a–5c for $M_\infty = 1.2$, respectively. The effects of the radius of the cone apex, the shoulder radius, and the fineness ratio are discussed in the following sections.

A. Base-First Entry Aerodynamics ($\alpha = 90$–180 deg)

1. Radius of Cone Apex (Apollo and Case 1)

The difference in the configurations of Apollo and case 1 is the radius of the cone apex. Little difference of the aerodynamic characteristics is observed for the base-first conditions as expected.Therefore, no result is shown here.

2. Shoulder Radius (Apollo and Case 2b)

Shoulder radius has significant effects on the base-first entry aerodynamics as can be seen in Figs. 4 and 5. $(C_L)_{\max}$ of case 2b is approximately half of the Apollo's. The computed pressure distributions and near-surface streamlines are shown in Figs. 6a and 6b for each geometry.

The separation line of the Apollo is essentially fixed at the shoulder because of its small shoulder radius, whereas the separation line of case 2b is not fixed at the shoulder. The high-pressure region appears in the base region, and this creates high lift for Apollo. On the other hand, there exists a high-pressure region (O_1-D in Fig. 6b) that creates a downforce for case 2b. Consequently, C_L for case 2b becomes smaller than that of Apollo at $\alpha = 120$–180 deg. This movement of the separation line also causes a slight difference in the C_{ma} characteristics as shown in Figs. 4c and 5c, resulting in the change of the longitudinal stability characteristics.

C_D of case 2b is much smaller than that of Apollo at $\alpha = 144$–180 deg for both $M_\infty = 0.9$ and 1.2. At $M_\infty = 0.9$, $\alpha = 180$ deg, C_D of case 2b is about 30% smaller than that of Apollo. This is because of the difference in the wind-side pressure distributions near the shoulder in the base region and the difference in the lee-side pressure level. The lee-side pressure level is relatively high in case 2b as compared to that of Apollo. The effect of the shoulder radius on the $(C_{D0})_{\alpha 180}$ will be discussed later.

3. Fineness Ratio (Apollo and Case 3b)

As Apollo and case 3b have the same base geometry, the aerodynamic characteristics at $\alpha = 144$–180 deg are almost the same.

The computed pressure distributions for Apollo and case 3b at $M_\infty = 1.2$, $\alpha = 144$ deg are shown in Fig. 7. The high-pressure region appears on the windward cone part because it is exposed to the freestream at this condition. Its pressure level of case 3b is higher, and its size is larger than that of Apollo, so that the downforce acting on this region is larger for case 3b, and C_L for case 3b becomes smaller. Therefore, the aerodynamic coefficients of Case 3b start deviating from Apollo's at around $\alpha = 144$ deg for $M_\infty = 0.9$ and around $\alpha = 156$ deg for $M_\infty = 1.2$. As the cone half-angle of case 3b is smaller than that of Apollo, the aerodynamic coefficients tend to be influenced by the downforce at earlier angles of attack than Apollo, and this influence comes out earlier when M_∞ is high.

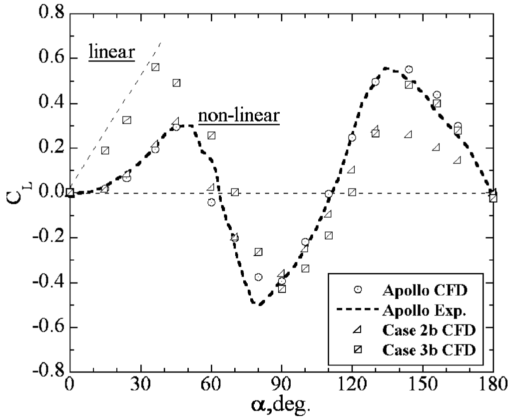

a) Lift coefficient

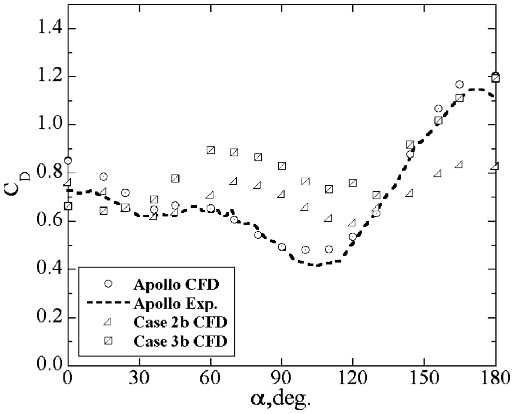

b) Drag coefficient

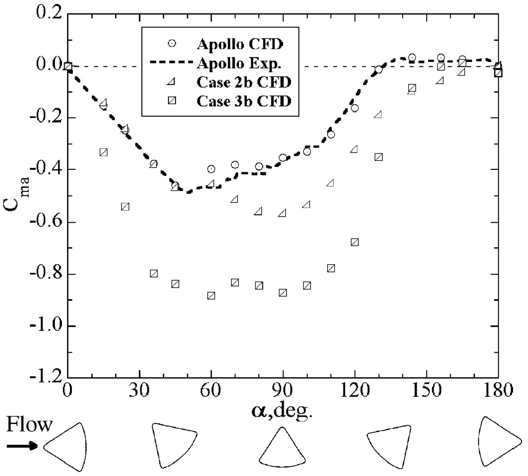

c) Pitching-moment coefficient

Fig. 4 Computed aerodynamic coefficients of Apollo, cases 2b and 3b at $M_\infty = 0.9$.

C_{ma} of case 3b begins to rapidly decrease at $\alpha = 144$ deg for $M_\infty = 0.9$ and at $\alpha = 156$ deg for $M_\infty = 1.2$, as the downforce acting on the windward cone part creates large magnitude of the pitching moment.

C_D of case 3b is larger than that of Apollo at $\alpha = 90$–130 deg as shown in Figs. 4b and 5b. This occurs simply because of the

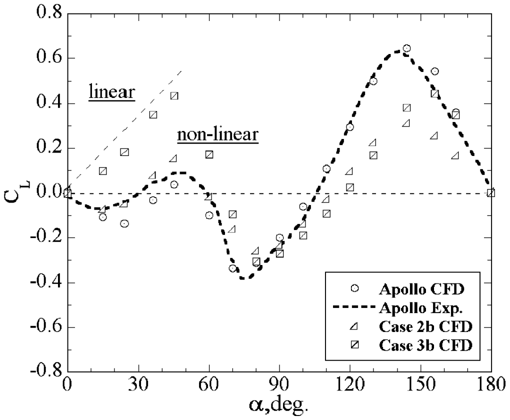

a) Lift coefficient

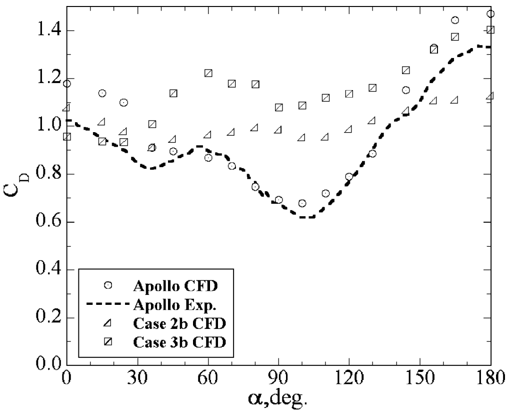

b) Drag coefficient

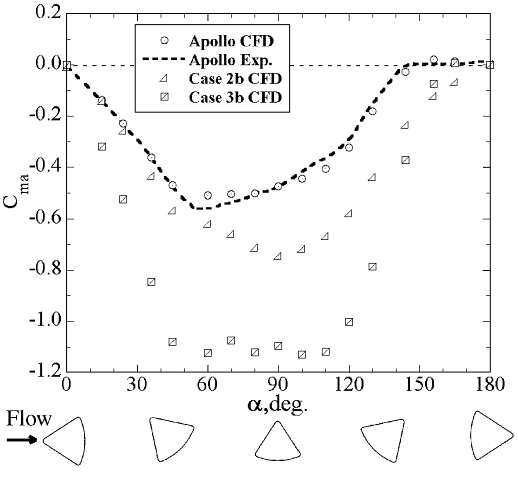

c) Pitching-moment coefficient

Fig. 5 Computed aerodynamic coefficients of Apollo, cases 2b and 3b at $M_\infty = 1.2$.

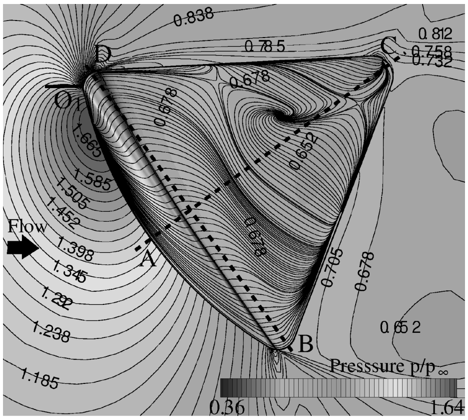

a) Apollo at $M_\infty = 0.9$, $\alpha = 144$ deg

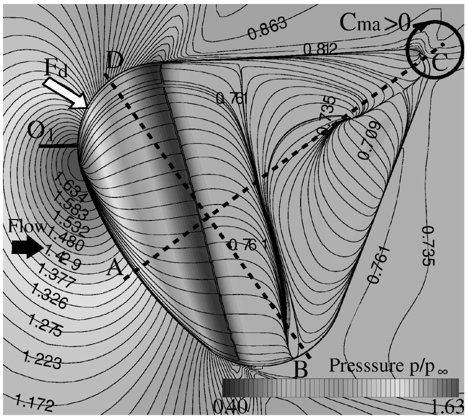

b) Case 2b at $M_\infty = 0.9$, $\alpha = 144$ deg

Fig. 6 Computed pressure p/p_∞ distributions on the surface and in the symmetry plane and surface flow pattern.

difference in the area of projection and can be explained by the Newtonian impact theory. The area of the projection is plotted for each configuration in Fig. 8. The projected area for case 3b has maximum value at $\alpha = 120$ deg, and it is 1.5 times larger than that for Apollo at the same angle of attack.

B. Nose-First Entry Aerodynamics ($\alpha = 0$–90 deg)

1. *Radius of Cone Apex (Apollo and Case 1)*

Computed aerodynamic coefficients C_A, C_N, and C_{ma} of Apollo and case 1 are compared in Fig. 9 for $M_\infty = 0.90$ and 1.20. Little differences are observed in all aerodynamic coeffients. It seems that the radius of the cone apex influences especially the C_A characteristics. However, C_A variation of case 1 is almost identical with that of Apollo. The radius of the cone apex has an effect only on the pressure distribution near the cone apex. It does not cause a significant change of the flow structures, such as the strength of the detached shock wave at supersonic conditions. It turns out that the aerodynamic characteristics are insensitive to the change of the radius of the cone apex.

2. *Shoulder Radius (Apollo and Case 2b)*

Little effects of the shoulder radius on the aerodynamic characteristics are observed for the nose-first conditions. Therefore, no discussions are shown here.

3. *Fineness Ratio (Apollo and Case 3b)*

Effect of the fineness ratio exists in all aerodynamic coefficients at all angles of attack, $\alpha = 0$–90 deg as shown in Figs. 4 and 5.

C_L of case 3b is about three times larger than that of Apollo at $\alpha = 0$–40 deg and linearly changes with α, while C_L of Apollo show nonlinear behavior at $\alpha = 0$–40 deg as shown in Figs. 4a and 5a. Comparison of the surface-pressure distributions and surface flow pattern between Apollo and case 3b at $M_\infty = 0.9$, $\alpha = 36$ deg is shown in Figs. 10a and 10b. The high-pressure region appears on the windside (B-C in Figs. 10a and 10b). Because cone half-angle of case 3b is smaller than that of Apollo, the size of the high-pressure region of case 3b and its contribution to the lift is larger than that of Apollo. This is the main reason for the larger C_L in case 3b.

The surface-pressure distributions of Apollo in the symmetry plane are shown in Fig. 11, along the A-D line shown in Fig. 10a The pressure level in the base region B-A-D and the lee-side cone part C-D at $M_\infty = 1.2$ significantly decreases as compared to that at $M_\infty = 0.9$. Consequently, C_L of Apollo at $\alpha = 36$ deg significantly decreases from 0.20 to -0.025 when M_∞ decreases from 0.90 to 1.20. The nonlinear behavior of C_L variation strongly depends on complicated these pressure changes.

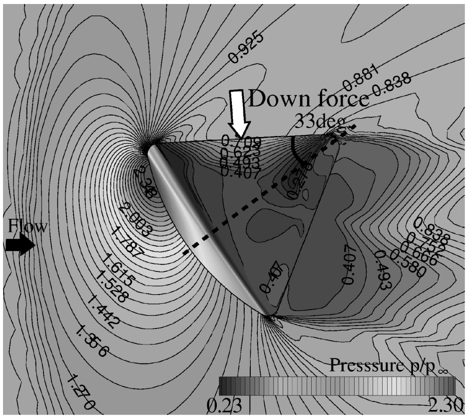

a) Apollo at $M_\infty = 1.2$, $\alpha = 144$ deg

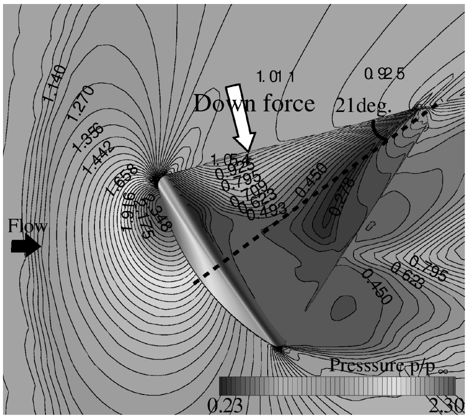

b) Case 3b at $M_\infty = 1.2$, $\alpha = 144$ deg

Fig. 7 Computed pressure distributions p/p_∞ on the surface and in the symmetry plane.

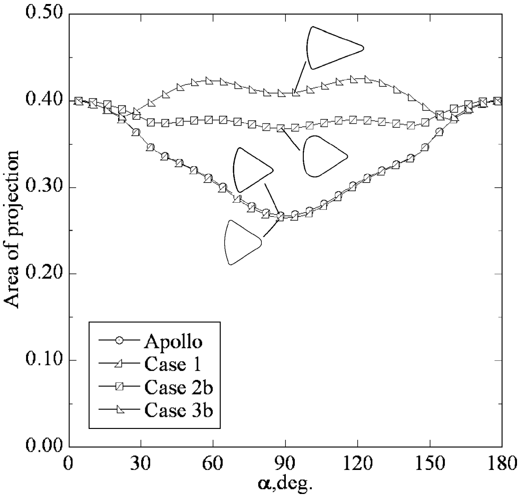

Fig. 8 Area of the surface of projection of Apollo, cases 2b and 3b.

C_{ma} of case 3b has larger magnitude as compared to that of Apollo. This is mainly because in case 3b the contribution of the aerodynamic force acting on the wind-side high-pressure region to C_{ma} is larger than that of Apollo.

There exist large differences in the variation of C_D for case 3b and Apollo at $M_\infty = 1.2$, as shown in Fig. 5a. This can be explained by the Newtonian impact theory: there exists differences in the area of the projection and the direction of the normal vector of the surface to the freestream direction.

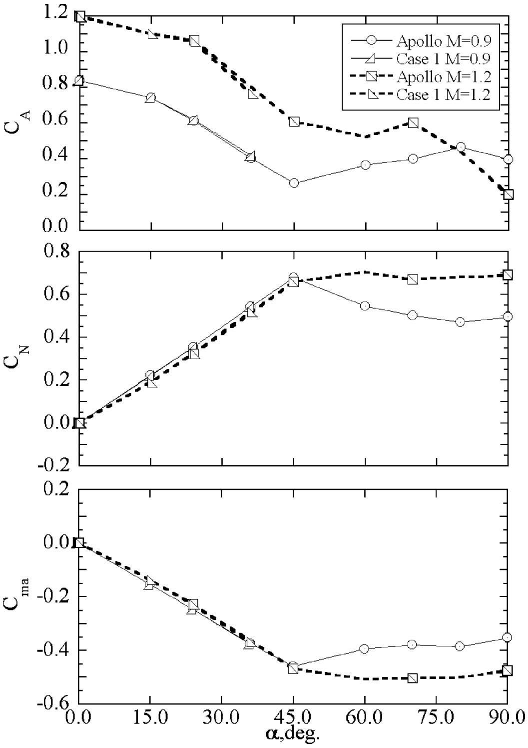

Fig. 9 Computed aerodynamic coefficients of Apollo and case 1.

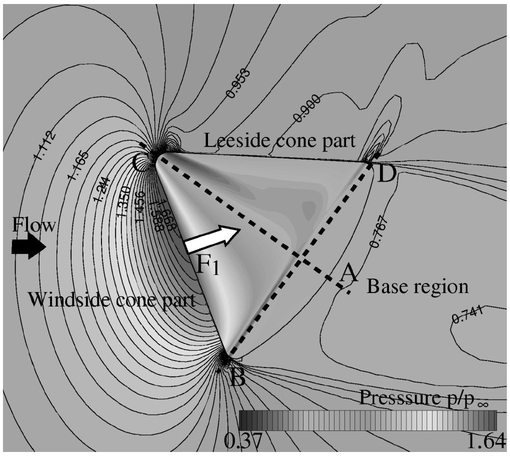

a) Apollo at $M_\infty = 0.9$, $\alpha = 36$ deg

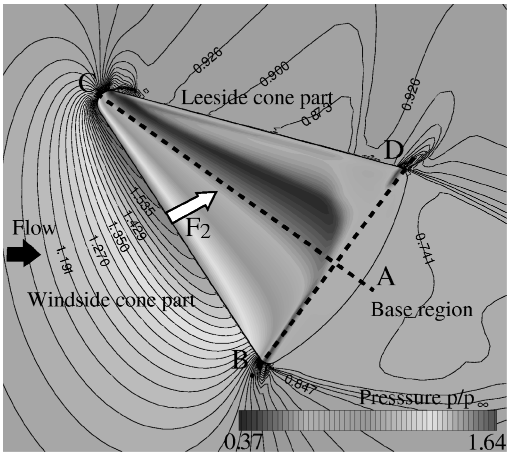

b) Case 3b at $M_\infty = 0.9$, $\alpha = 36$ deg

Fig. 10 Computed pressure distributions p/p_∞ and surface flow pattern.

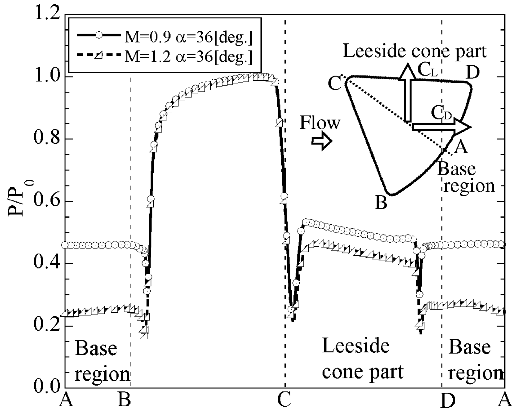

Fig. 11 Computed pressure distributions at Apollo at $\alpha = 36$ deg, $M_\infty = 0.9, 1.2$.

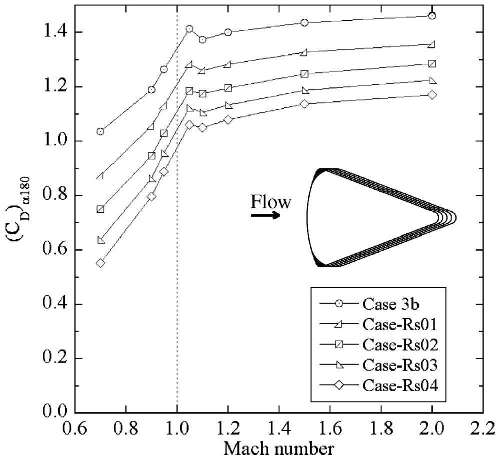

a) Computed $(C_{D0})_{\alpha180}$

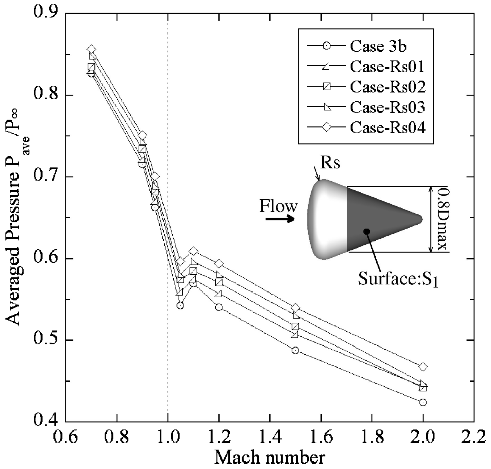

b) Averaged lee-side pressure at $\alpha = 180$ deg

Fig. 12 Shoulder radius effect on the $(C_{D0})_{\alpha180}$.

Table 2 Flow conditions for cases 3a-1–3a-4

Parameter	Value
M_∞	0.70, 0.90, 0.95, 1.05, 1.10, 1.20, 1.50, 2.00
Re_∞	1.0×10^6
α	180.0 deg

Table 3 Flow conditions for cases TH15, TH21, TH27, and Apollo

Parameter	Value
M_∞	0.6, 0.7, 0.8, 0.9, 0.95, 1.1, 1.15, 1.2, 1.3, 1.4, 1.5, 1.65, 1.8, 2.0
Re_∞	1.0×10^6
α	0.0 deg

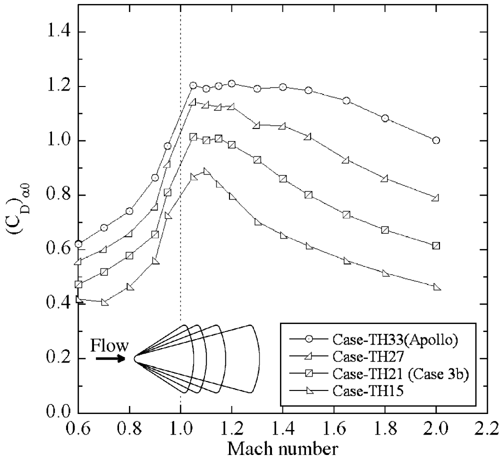

Fig. 13 Fineness ratio effect on the $(C_{D0})_{\alpha0}$.

C. Shoulder Radius Effect on the $(C_{D0})_{\alpha180}$

Effect of the shoulder radius on the $(C_{D0})_{\alpha180}$ is also investigated for the four additional configurations, cases Rs01–Rs04 having different shoulder radius but having all other parameters equal to those of case 3b. Flow conditions are listed in Table 2. Computed $(C_{D0})_{\alpha180}$ are shown in Fig. 12a. Averaged lee-side pressure P_{ave} acting on the S1 surface is plotted against Mach numbers in Fig. 12b. S1 is defined in the same figure. P_{ave} for all of the configurations rapidly decreases linearly until the freestream becomes supersonic. After the freestream becomes supersonic, P_{ave} still continues to decrease, but its variation becomes gradual. The variation in the $(C_{D0})_{\alpha180}$ with M_∞ is strongly related to the variation in the P_{ave}. This figure also shows that the configurations with larger shoulder radius have smaller $(C_{D0})_{\alpha180}$ at all of the M_∞. $(C_{D0})_{\alpha180}$ decreases by roughly 0.05~0.1 when the shoulder radius becomes two times larger. In total, the shoulder radius has strong effect on the lee-side pressure distributions so that the aerodynamic force changes especially in the axial direction.

D. Fineness Ratio Effect on the $(C_{D0})_{\alpha0}$

Effects of the fineness ratio on the $(C_{D0})_{\alpha0}$ characteristics are also investigated for the four types of configurations, Apollo, and cases TH15, TH21, and TH27. Flow conditions are listed in Table 3. Computed $(C_{D0})_{\alpha0}$ are shown in Fig. 13. $(C_{D0})_{\alpha0}$ of all the configurations rapidly increase until the freestream becomes supersonic. Once the freestream becomes supersonic, $(C_{D0})_{\alpha0}$ takes its peak value and begins to decrease gradually with M_∞. M_∞ for the peak $(C_{D0})_{\alpha0}$ is 1.05 or 1.10. In addition, $(C_{D0})_{\alpha0}$ is larger at all of the Mach numbers for the geometry having the small fineness ratio, $(C_{D0})_{\alpha0}$ increases by roughly 0.1 at subsonic conditions and 0.2 at supersonic conditions when cone half-angle increases by 6 deg.

Averaged lee-side pressure P_{ave} acting on the S2 surface is plotted against Mach numbers in Fig. 14a. S2 is defined in the same figure. As shown in Fig. 14a, fineness ratio has little effects on the lee-side base pressure level. On the other hand, fineness ratio has significant effects on the wind-side pressure distributions. The surface-pressure distributions in the symmetry plane at $M_\infty = 0.12$, $\alpha = 0$ deg is shown in Fig. 14b for each geometry. At the supersonic flow conditions, the detached shock wave for the geometry of smaller fineness ratio is stronger, resulting in the higher wind-side pressure distributions as shown in Fig. 14b Consequently, $(C_{D0})_{\alpha0}$ of the geometry with smaller fineness ratio becomes larger.

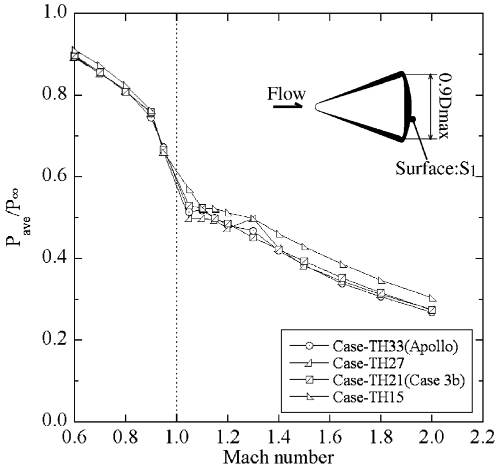

a) Averaged lee-side pressure at $\alpha = 0$ deg

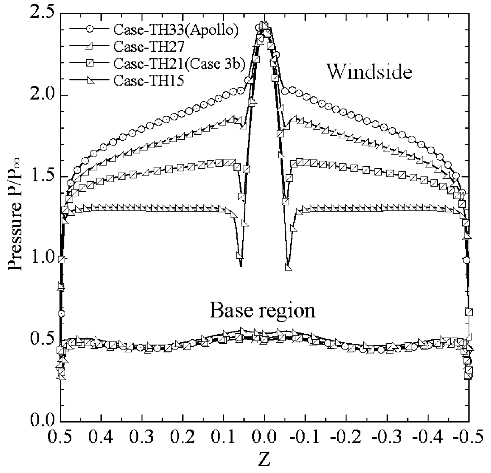

b) Surface-pressure distributions in the symmetry plane at $M_\infty = 1.2$, $\alpha = 0$ deg

Fig. 14 Fineness ratio effect on surface-pressure distributions at $\alpha = 0$ deg.

IV. Conclusions

Flowfields around Apollo-type conical configurations were numerically simulated, and their aerodynamic characteristics were obtained by Reynolds-averaged Navier–Stokes computations at a wide range of angles of attack under subsonic through supersonic flows. Futhermore, effects of the configuration parameters on the aerodynamic characteristics and their flow mechanisms were clarified based on the computed results. The following observations can be drawn from the results.

The aerodynamic characteristics hardly change when the radius of the cone apex becomes two times larger than that of Apollo. The radius of the cone apex has little effect on the aerodynamic characteristics.

The shoulder radius strongly influences the position of the separation line and the pressure level behind the body. For the configurations with large shoulder radius, the increase of the pressure level behind the body leads to the reduction of drag, and the movement of the separation line generates the downforce.

At the base-first entry conditions, when the fineness ratio is large, the high-pressure region appears on the cone surface by the influence of the freestream. The downforce is generated in this region, resulting in small C_L as compared to that for the geometry, which has a smaller fineness ratio. On the other hand, at the nose-first entry conditions C_L becomes larger as the aerodynamic force acting on the wind-side high-pressure region mainly contributes to the lift. C_{ma} becomes larger for the geometry, which has larger fineness ratio in both angles-of-attack conditions as the contribution of the aerodynamic force acting on the high-pressure region to the C_{ma} is larger. The fineness ratio has little effect on the lee-side pressure level, although it has significant effect on the wind-side pressure distributions.

Acknowledgment

This study was partially supported by Grant-in-Aid 13450400 from the Ministry of Education, Culture, Sports, Science and Technology of Japan.

References

[1] "Access to Space Study, Summary Report," NASA TM-109693, Jan. 1994.

[2] Kelly, J. M., Robert, J. N., Richard, A. T., Brian, R. H., and Ramadas, P., "X-33 Hypersonic Aerodynamic Characteristics," *Journal of Spacecraft and Rockets*, Vol. 38, Np. 5, 2001, pp. 670–683.

[3] Blase, W. P., "The First Reusable SSTO Spacecraft," *Spaceflight*, Vol. 35, No. 3, 1993, pp. 90–94.

[4] Inatani, Y., Naruo, Y., and Yonemoto, K., "Concept and Preliminary Flight Testing of Fully Reusable Rocket Vehicle," *Journal of Spacecraft and Rockets*, Vol. 38, No. 1, 2001, pp. 36–42.

[5] Woods, W. C., and Merski, N. R, "Aerodynamic Characteristics of a Vertical Takeoff Vertical Landing (VTVL) Single Stage to Orbit Vehicle from $M_\infty = 0.1$ to 10," AIAA Paper 95-1828, June 1995.

[6] Fujimoto, K., and Fujii, K., "CFD Prediction of the Aerodynamic Characteristics of Capsule-Like Configurations for Future SSTO Development," AIAA Paper 03-0912, Jan. 2003.

[7] Fujimoto, K., and Fujii, K., "Compressible Flow Simulations over Basic Reusable Rocket Configurations," American/Japan Society of Mechanical Engineers, Paper FEDSM 2003-45427, July 2003.

[8] Fujimoto, K., and Fujii, K., "Assesment of CFD Estimation of Aerodynamic Characteristics of Basic Reusable Rocket Configurations," *Transactions of the Japan Society for Aeronautical and Space Sciences*, Vol. 48, No. 159, 2005, pp. 13–20.

[9] Moseley, W. C., Jr., Moore, R. H., Jr., and Hughes, J. E., "Stability Characteristics of the Apollo Command Module," NASA TN D-3890, March 1967.

[10] Shima, E., and Jounouchi, T., "Role of CFD in Aeronautical Engineering (No14)-AUSM Type Upwind Schemes-," *Proceedings of the 14th NAL Symposium on Aircraft Computational Aerodynamics*, Inst. of Aerospace Technology, Tokyo, 1997, pp. 7–12.

[11] van Leer, B., "Toward the Ultimate Conservative Difference Scheme. 4, A New Approach to Numerical Convection," *Journal of Computational Physics*, Vol. 23, No. 3, 1977, pp. 276–299.

[12] Fujii, K., "Practical Applications of New LU-ADI Scheme for the Three-Dimensional Navier–Stokes Computation of Transonic Viscous Flows," AIAA Paper 86-0513, Jan. 1986.

[13] Baldwin, B., and Lomax, H., "Thin Layer Approximation and Algebraic Model for Separated Turbulent Flows," AIAA Paper 78-257, Jan. 1978.

[14] Fujii, K., and Obayashi, S., "High-Resolution Upwind Scheme for Vortical-Flow Simulation," *Journal of Aircraft*, Vol. 26, No. 12, 1989, pp. 1123–1129.

[15] Ogawa, T., and Fujii, K., "Numerical Investigation of Three-Dimensional Compressible Flows Induced by a Train Moving into a Tunnel," *Computers and Fluids*, Vol. 26, No. 6, 1997, pp. 565–585.

[16] Fujii, K., and Obayashi, S., "Navier–Stokes Simulations of Transonic Flows over a Practical Wing Configuration," *AIAA Journal*, Vol. 25, No. 3, 1987, pp. 369, 370.

[17] Fujimoto, K., and Fujii, K., "Computational Prediction of the Aerodynamic Characteristics of SSTO Vehicle Configurations," Inst. of Space and Astronautical Sciences, Rept. 682, Kanagawa, Japan, Sept. 2003.

R. Cummings
Associate Editor